To cite this version :

Rubber Impact on 3D Textile Composites

**Sebastian Heimbs · Björn Van Den Broucke ·
Yann Duplessis Kergomard · Frederic Dau ·
Benoit Malherbe**

Abstract A low velocity impact study of aircraft tire rubber on 3D textile-reinforced composite plates was performed experimentally and numerically. In contrast to regular unidirectional composite laminates, no delaminations occur in such a 3D textile composite. Yarn decohesions, matrix cracks and yarn ruptures have been identified as the major damage mechanisms under impact load. An increase in the number of 3D warp yarns is proposed to improve the impact damage resistance. The characteristic of a rubber impact is the high amount of elastic energy stored in the impactor during impact, which was more than 90% of the initial kinetic energy. This large geometrical deformation of the rubber during impact leads to a less localised loading of the target structure and poses great challenges for the numerical modelling. A hyperelastic Mooney-Rivlin constitutive law was used in Abaqus/Explicit based on a step-by-step validation with static rubber compression tests and low velocity impact tests on aluminium plates. Simulation models of the textile weave were developed on the meso- and macro-scale. The final correlation between impact simulation results on 3D textile-reinforced composite plates and impact test data was promising, highlighting the potential of such numerical simulation tools.

Keywords 3D textile composite · Rubber impact · Damage mechanisms · Numerical simulation

S. Heimbs (✉) · B. Van Den Broucke
EADS Innovation Works, 81663 Munich, Germany
e-mail: sebastian.heimbs@eads.net

Y. Duplessis Kergomard · F. Dau
LAMEFIP, Arts et Métiers ParisTech, Université Bordeaux 1, 33405 Talence Cedex, France

B. Malherbe
Airbus, 316 Route de Bayonne, 31060 Toulouse Cedex 03, France

1 Introduction

Composite materials are more and more used in primary and secondary aircraft structures due to their well-known advantages in terms of weight-specific stiffness and strength or fatigue performance. However, as the reinforcing fibres are mostly oriented in the laminate plane, composites are vulnerable against transversal impact loads. In common unidirectional ply laminates there is no reinforcement in thickness direction and transversal impact loads may typically lead to the separation of individual plies (delamination), which can reduce the overall stiffness and residual strength of the component.

One promising measure in this context is the use of 3D fibre-reinforced composites. 3D reinforcements can be manufactured in a number of different ways, e.g. stitching, tufting, 3D braiding or 3D weaving [1]. The current study focuses on 3D textile weaves, where yarns are interlaced in a manner similar to 2D woven fabrics, except that the warp yarns may penetrate more than one layer of weft yarns (through-the-thickness angle interlock weave, Fig. 1). In several previous studies it could be proven that no delaminations occur in such 3D textile-reinforced composites under transversal impact and their impact performance is superior compared to 2D textile composites [2–4].

Several impact scenarios on aircraft structures are possible, ranging from low velocity impacts (e.g. the classical tool drop during maintenance work) to high velocity impacts (e.g. runway debris, bird strike, hail during flight, fan blade-off etc.). One of these relevant scenarios is tire rubber impact from a bursting tire. This very load case led to the fatal accident of Concorde flight 4590 near Paris in the year 2000, where a piece of tire rubber was thrown against the fuel tank, causing a fuel valve to burst and initiating an engine fire [5]. Rubber impacts are different in nature compared to hard body impacts from stones or metal pieces, resulting from the highly elastic material response. Different studies have investigated tire rubber impacts on metallic aircraft structures in the past, both experimentally and numerically [6–9]. Also rubber impact simulations on stringer-stiffened laminated composite panels have been performed [10, 11]. However, no previous study covers the performance of 3D textile composites under rubber impact.

The current investigation is intended to fill this gap. It was performed within the project VULCOMP (Vulnerability of Composite Structures, 2007–2010), which addresses the impact performance of 3D textile composites. The aim is to characterise the damage mechanisms under transversal impact by a rubber body based on experimental test series and non-destructive and destructive inspection methods. Furthermore, numerical simu-
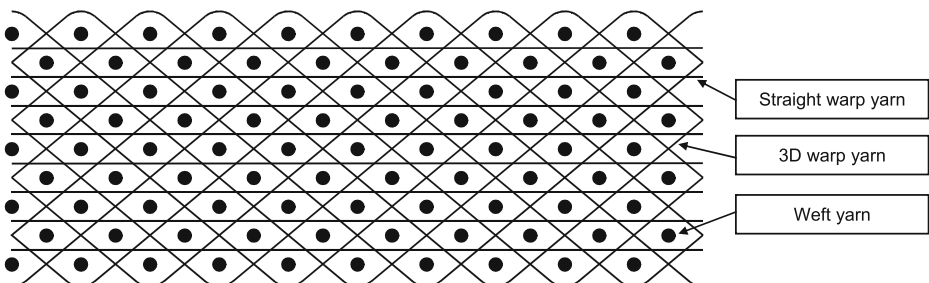

Fig. 1 Illustration of through-the-thickness angle interlock (3X) weave

lations based on the finite element (FE) method are adopted that allow for numerical analyses of the textile composite on the meso- and macro-level.

2 Experimental Part

2.1 Materials

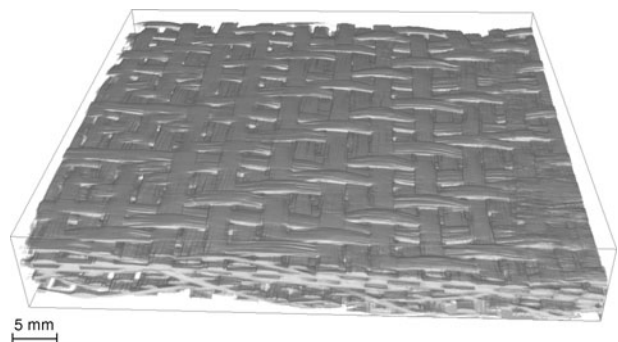#### 2.1.1 3D Textile Composite Material

The composite material under study is a 3D carbon fibre textile weave impregnated with epoxy resin. The through-the-thickness angle interlock (3X) weave with an areal weight of 2,720 g/m² is made of Tenax-E HTS 40F13 12K yarns in both warp and weft directions and was manufactured by CTMI, La Sône (FR). A total of three different 3D reinforcement patterns have been investigated in this study with different ratios of 3D warp yarns to straight warp yarns (Fig. 1): 30%, 55% and 100%. This paper will concentrate on the results of the 3X 55% material, though. A three-dimensional micro-computer-tomography (micro-CT) scan of the dry 3X 55% material is shown in Fig. 2 to give an impression of the textile weave. Hexcel RTM6 epoxy resin was used to manufacture the composite plates with the resin transfer moulding (RTM) process at CRITT, Toulouse (FR). The resin was injected at 120°C and the composite plate was cured at 160°C. The final thickness of the composite plate was 2.7 mm.

2.1.2 Rubber Impactor Material

The impactor in this study is made from styrene-butadiene-styrene (SBS) rubber, which is a hard and durable rubber material typically used for aircraft tire treads or shoe soles. SBS rubber impactors with three different Shore A hardness values (SHA) were selected for this study and manufactured by SMAC, Toulon (FR): SHA-40, SHA-60 and SHA-80.

The impactor geometry was chosen to be of simple regular and symmetrical shape in order to reduce the complexity of this study. For this reason, a hemispherical rubber impactor geometry was selected. The hemispherical piece of rubber was bonded to a steel cylinder with a height of 22 mm that is mounted to the carriage of the drop tower test rig (Fig. 3). A total of three different diameters were used in this study: 40 mm,

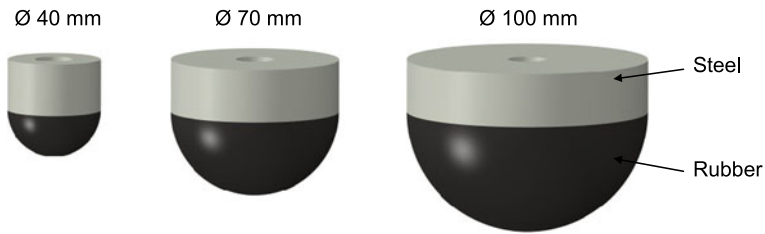Fig. 2 Micro-CT scan of 3D textile weave (3X 55%)

5 mm

Fig. 3 Overview of rubber impactors with three different diameters

70 mm and 100 mm. The focus of the impact tests in this paper will be on the 40 mm impactor, though.

2.2 Coupon Tests of 3D Textile Composite for Elastic and Damage Properties

2.2.1 Tensile Tests in Warp (0°) and Weft (90°) Direction

In order to determine the mechanical properties of the 3X 55% textile composite quasi-static coupon tests were performed on a Zwick universal testing machine. Test coupons of the dimensions 300 mm×32 mm×2.7 mm according to Airbus test method AITM 1-0007 were cut on a high precision water jet machine. Glass fibre composite end tabs with a length of 60 mm were bonded onto both ends for load introduction and clamping purposes. All tests were performed at room temperature with a cross-head speed of 2 mm/min.

The tensile tests were performed in warp (0°) and weft (90°) direction of the textile composite with three specimens for each test. Two strain gauges were applied on each specimen measuring the longitudinal and transversal strains in the linear elastic region. Poisson's ratio and Young's modulus were determined in this linear elastic regime between 0.05% and 0.25% tensile strain.

The Young's modulus in weft direction with a mean value of $E_{2+}=68.88$ GPa is only slightly lower than in warp direction with $E_{1+}=69.54$ GPa. The strength, however, is much lower with mean values of $\sigma_{2+}=440$ MPa and $\sigma_{1+}=605$ MPa, respectively. In warp direction there is a slight nonlinearity up to the strength value, starting at strain values of
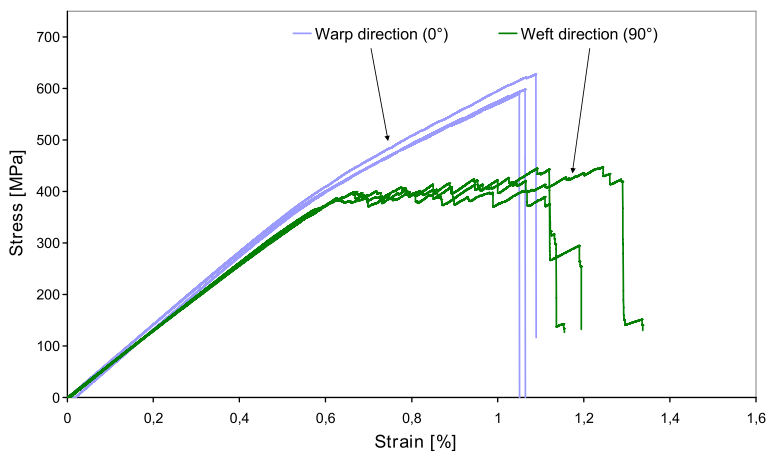

Fig. 4 Stress-strain curves of 3X 55% for tensile tests in warp (0°) and weft (90°) direction

approx. 0.6%. In weft direction, after strains of 0.6%, the material shows significant fibre-matrix debonding under oscillating loads until the specimen breaks (Fig. 4).

2.2.2 Cyclic 45° Tensile Tests

Cyclic tensile tests were performed in 45° direction in order to characterise the resin-dominated nonlinear damage behaviour under in-plane shear loading. For these tests a precise measurement of the longitudinal and transversal strains is necessary in order to calculate the shear strains in the linear and nonlinear regime. Strain gauges or a laser-extensometer are insufficient for this purpose as they measure at one specific location only, which might not necessarily be the location of damage. Damage may initiate at one local area during the test and exactly there the measurement has to take place. Optical strain measurement using the Aramis system was regarded as the best method in this case, which allows for strain evaluations on every position of the specimen. A total number of five specimens were tested with about 12 cycles before failure (Fig. 5a). Based on the images taken of the specimen with a high contrast surface pattern during the test, virtual strain gauges can be applied within the Aramis software to measure the longitudinal and transversal strains in the area where the specimen fails. With the known values of force F, specimen width w, thickness t and strains ε_1 and ε_2, the shear stress-shear strain curve can be plotted using the equations from Airbus test method AITM 1-0002 for 45° tensile tests (Fig. 5b):

$$\sigma_{12} = \frac{F}{2wt} \tag{1}$$

$$\varepsilon_{12} = \varepsilon_1 - \varepsilon_2 \tag{2}$$

2.3 Rubber Compression Tests

The compressive behaviour of the SBS rubber impactors was determined in quasi-static compression tests on a 10 kN universal testing machine using two different cross-head
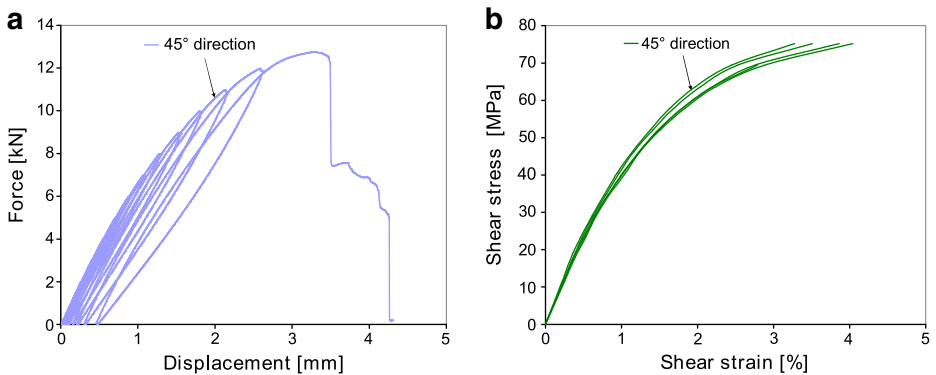

Fig. 5 Test results of cyclic 45° tensile tests of 3X 55% composite material: **a** force-displacement curve and **b** shear stress-shear strain curve

speeds, 5 mm/min and 50 mm/min. The hemispherical impactors shown in Fig. 3 were compressed uniaxially on a rigid surface. All three impactor diameters (Ø40 mm, Ø70 mm, Ø100 mm) and all three hardness values (SHA-40, SHA-60, SHA-80) were tested. The force-displacement diagrams are shown in Fig. 6. It shall be noted that for each Shore hardness the force-displacement curves of all three impactor diameters matched.

2.4 Rubber Impact Tests on Aluminium Plate

As a next step, the dynamic compression properties of the rubber were determined in low velocity impact tests on metallic plates. At the same time, these tests were intended to be a source for the numerical validation of the impactor model. A 5 mm thick 2024-T3 grade aluminium plate was selected as the target structure, since the mechanical behaviour of such a plate is well-known and straight-forward to model. With this deformable target, having a comparable stiffness as the composite plates, the impactor performance can be assessed in a comparable manner as in the later tests on composite plates, which is important since the impactor deformation depends on the target structure stiffness. This was the reason for the decision against a rigid target structure for these tests.

The low velocity impact tests were performed on a drop tower using drop heights of 1 m and 2 m, leading to impact velocities of 4.1 m/s and 5.9 m/s. These are the measured velocities, which are slightly lower than the theoretically predicted values due to friction losses at the carriage cylinders of the drop tower. The total mass of the carriage including the rubber impactor was 5.3 kg, leading to impact energies of approx. 50 J and 100 J. The aluminium plates of 100 mm×100 mm×5 mm were clamped in an aluminium frame with a circular opening of Ø70 mm and fixed by four bolts on all four corners.

The impact force was measured by a piezoelectric sensor of the type Kistler 9061A. The carriage displacement as well as the plate deflection were recorded by a laser sensor. All tests were recorded with an APX RS high speed camera with an acquisition speed of 10,000 img/s to assess the impactor deformation. The acquisition frequency of force, carriage displacement and plate deflection was 30,000 Hz.

The deformation of the Ø40 mm SHA-60 rubber impactor during the impact on the aluminium plate is shown in Fig. 7 with images taken from the high speed video. The elastic deformation of the rubber material especially for the impact energy of 100 J is significant.
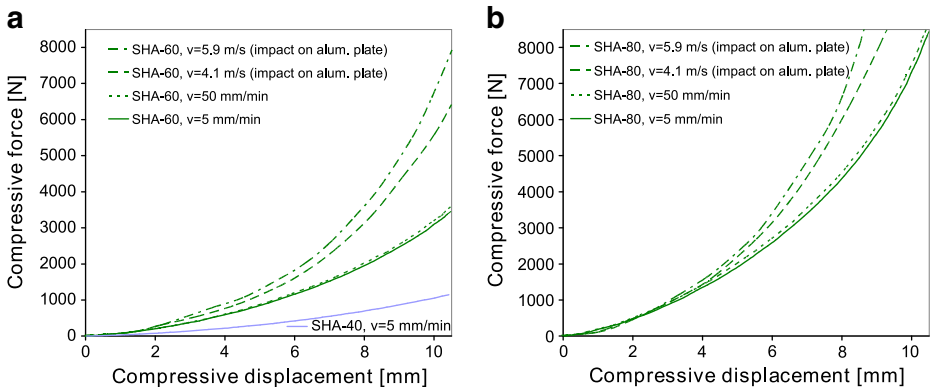

Fig. 6 Compressive force-displacement curves of **a** SHA-40 and SHA-60 rubber, **b** SHA-80 rubber
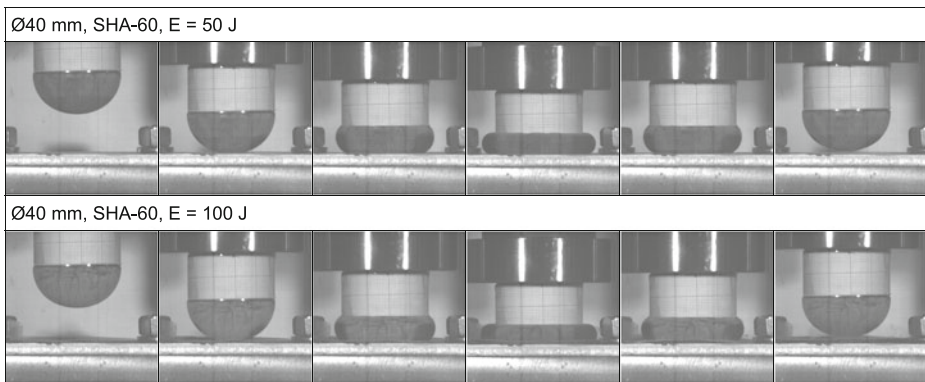
Fig. 7 Rubber impactor deformation during impact on aluminium plate taken from high speed video

The force-time plots of the SHA-60 and SHA-80 impactors are shown in Fig. 8a. It is interesting to note that for different hardness values the peak values are similar and only depend on the kinetic energy. However, the contact time is shorter for higher hardness values. The maximum force is twice as high for the higher impact energy.

The carriage displacement of the drop weight vs. time is given in Fig. 8b, indicating quantitatively the deformation of the rubber impactor. The difference of the compressive deformation between 50 J and 100 J of impact energy is only relatively small. The compressive deformation of rubber with higher hardness values is lower.

The force-displacement curves have been added to Fig. 6 to indicate the strain rate effect of the SBS rubber. However, it has to be noted that these curves do not result from tests on a rigid surface and therefore cannot directly be compared.

2.5 Rubber Impact Tests on 3D Composite Plate

The low velocity impact tests of rubber impactors on 3D textile composite plates have been performed with the same drop tower test setup as before for the impact tests on aluminium plates [12, 13]. The composite specimens had a dimension of 100 mm×100 mm×2.7 mm.
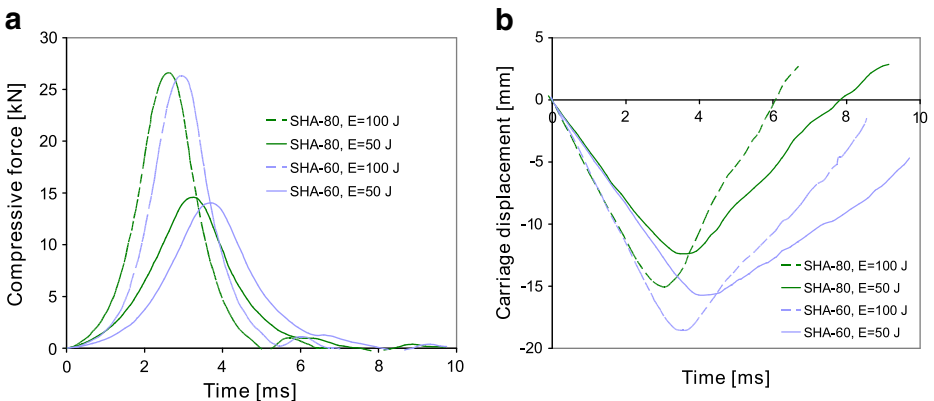

Fig. 8 a Force-time curves and b carriage displacement-time curves of SHA-60 and SHA-80 rubber impactors during impact on aluminium plate with impact energies of 50 J and 100 J

All three 3X reinforcement types with 30%, 55% and 100% 3D warp yarns were tested. However, this paper will focus on impact test results of the rubber impactor with a diameter of 40 mm and a Shore hardness of SHA-60. The composite specimen was clamped between two metallic plates with a circular window with a diameter of 70 mm, fixed by four bolts (Fig. 9). Five different drop height values were tested: 1 m, 1.25 m, 1.5 m, 1.75 m and 2 m, again leading to impact energies between 50 and 100 J.

The force-time and carriage displacement-time plots of the 3X 55% and 3X 100% composite materials for impact energies of 50 J and 100 J are shown in Fig. 10. The curves for both materials are very similar, the major difference can be seen in the force peak values for the highest impact energy. The oscillations in the curve for the 3X 55% material in the peak area indicate a higher extent of damage compared to the 3X 100% material.

For non-destructive damage inspection thermography scans were used that are able to show irregularities or fracture surfaces inside the material (Fig. 11). Damage starts at impact energies of 75 J and becomes severe for 100 J. Penetration did not occur for these energies, though. In a further test series it was found out that penetration of the plate occurs for energies higher than approx. 300 J, using a Ø70 mm SHA-60 impactor with a mass of 13.9 kg and a drop height of 2.25 m. It can be seen that the damage decreases with an increasing ratio of 3D warp yarns to straight warp yarns. The 3X 100% material has the lowest extent of damage, indicating that this material has the highest resistance against impact loads. Because the thermography images only allow for a global impression of the extent of damage but not for a detailed assessment of local damage mechanisms, micrographs have been taken from the impacted specimens showing the area between the centre of impact and the support (Fig. 12). The major modes of damage appear to be yarn decohesions, matrix cracks and few yarn ruptures. The decohesions appear to start at the back side of the plate centre and progress outwards to the direction of the boundary support. Large-scale delaminations as in unidirectional composite laminates do not occur because the composite consists of only one ply of the 3D textile weave.

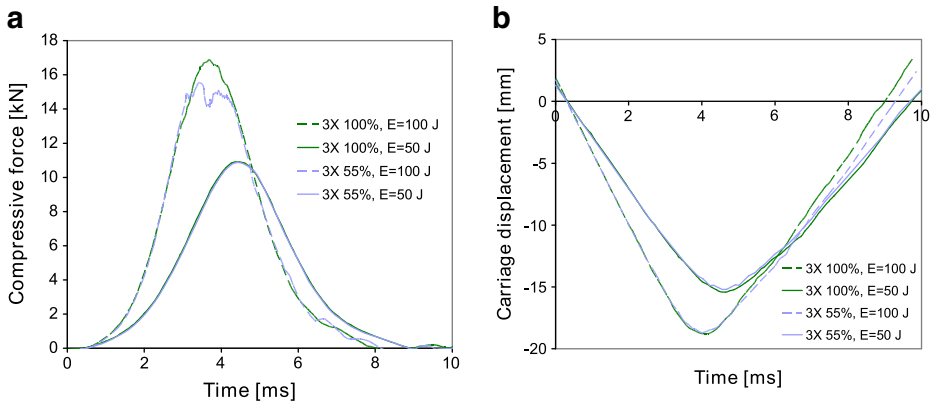**Fig. 9** Drop tower test setup for rubber impact on composite plates

Fig. 10 a Force-time curves and **b** carriage displacement-time curves of SHA-60 rubber impactor on composite plates with 55% and 100% 3D warp yarns for impact energies of 50 J and 100 J

3 Numerical Analysis

It is well-known that numerical methods based on the finite element (FE) method are an efficient tool in the structural development process, reducing the time and cost expenses of extensive experimental testing. The aim of current developments in aircraft engineering is to reduce the dimension of the experimental testing pyramid and to substitute it with efficient numerical simulations. Ideally, experimental tests shall only be used in a limited extend where they are necessary for validation or certification reasons. In the framework of
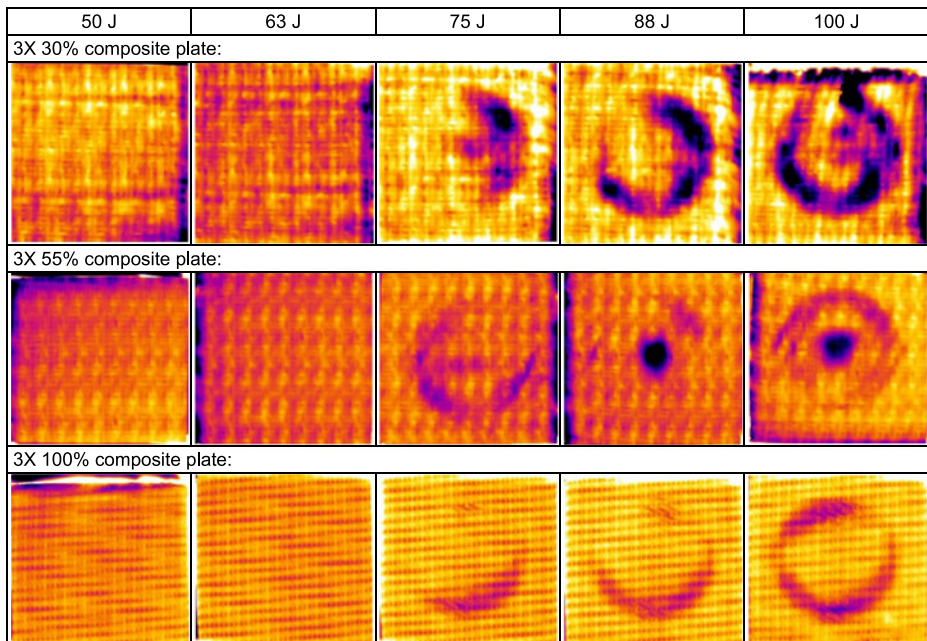

Fig. 11 Thermography inspection images after impact for composite plates with 30%, 55% and 100% 3D warp yarns
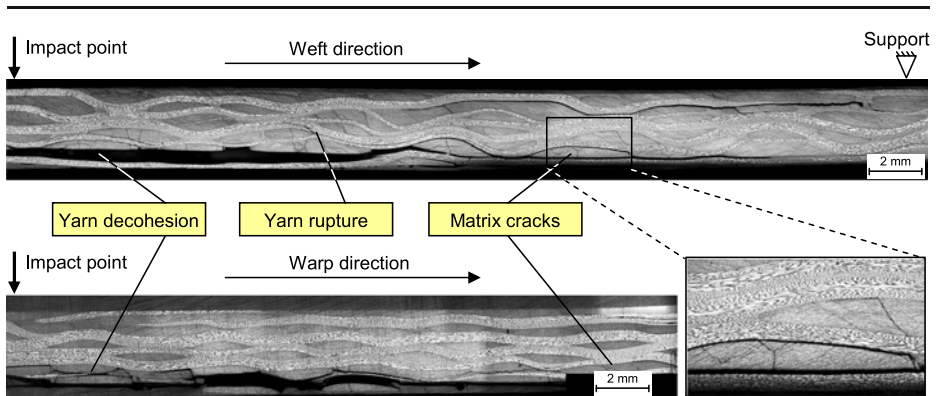
Fig. 12 Micrograph images after 100 J impact for 3X 55% composite plate

this study, impact simulation models were developed in the commercial FE-code Abaqus/Explicit 6.10 to assess the accuracy of such numerical analyses. Adequate models for both the rubber impactor and the textile composite plate had to be defined and validated first before performing the rubber impact simulations.

3.1 Rubber Impactor Modelling and Validation

For impact simulations it is not only necessary to have a reliable constitutive model of the target structure, but also to have an adequate and validated model of the impactor, so that the loads applied to the target structure during the time of impact are represented correctly. In this study, the impactor is made from rubber, which is a hyperelastic material with a rate-dependent constitutive behaviour. Such a rubber impact scenario is challenging as a significant amount of the initial kinetic energy is converted into elastic deformation of the projectile, so that the kinetic energy transferred to the target structure depends strongly on the interaction between plate and projectile.

Rubber and rubber-like materials may exhibit very large elastic strains, where the linear elastic Hooke law cannot accurately describe the observed constitutive behaviour anymore. These rubber materials are rather treated as hyperelastic, with the stress-strain behaviour being described by a strain energy potential, which defines the energy stored in the material per unit of volume of initial configuration as a function of the strain at that point of the material. Melvin Mooney and Ronald Rivlin developed the first hyperelastic material models independently from each other in the 1940s [14, 15]. Their phenomenological description, known as the Mooney-Rivlin model, is still one of the most accepted material models for rubber materials.

3.1.1 Literature Overview on Rubber Modelling

The rubber modelling activities in this study were begun with a literature overview, as several investigations on tire rubber impact have been performed in the past and can be found in the technical literature. In an early publication of Johnson, Kempe and Simon [16], the high velocity impact of an aircraft tire fragment, represented by an 1.47 kg rubber ball, on a composite CF/PEEK wing access cover panel was tested and simulated with the FE-code Pam-Crash. Thereafter, the impact of an aircraft tire fragment on an aluminium wing access cover panel was studied experimentally and numerically in the European FP5 project

CRAHVI (Crashworthiness of Aircraft for High Velocity Impact). A more complex and realistic rubber impactor was used, which was a real piece of aircraft tire tread with reinforcing cords. An impact simulation model was developed in LS-Dyna based on the hyperelastic Mooney-Rivlin material law without strain rate effects and one-dimensional bar elements for the reinforcements, which was used for high velocity impact simulations of large tire fragments on aluminium wing access cover panels [6–9]. More recently, in the European FP6 project ALCAS (Advanced Low Cost Aircraft Structures) tire rubber impact simulations on stringer-stiffened composite panels have been performed with Pam-Crash. Again, the hyperelastic Mooney-Rivlin material model was used for the 840 g rubber impactor [10, 11]. Other publications do not cover the impact of a tire fragment on an aeronautical structure, but describe approaches for tire rubber modelling for other purposes, mostly automotive-related topics. In [17] the low velocity impact of a rigid indenter on an automobile tire is studied, using Abaqus/Explicit and the hyperelastic Mooney-Rivlin material model. Strain rate effects were neglected. The material parameters were taken from the studies by Bolarinwa and Olatunbosun [18, 19], who assessed hyperelastic tire rubber modelling approaches in Abaqus/Explicit and performed a simulation of a bursting automobile tire with the Mooney-Rivlin material model. Detailed automobile tire models were also developed in [20] and [21] in the codes LS-Dyna and MSC.Marc, respectively. Both used the Mooney-Rivlin model for the rubber material. An aircraft tire was modelled in [22–24] using LS-Dyna and the Mooney-Rivlin model for the analysis of the lofting mechanism of small runway debris particles and stones by the rolling tire.

From this literature overview on tire rubber modelling and rubber impact modelling it can be concluded that the hyperelastic Mooney-Rivlin material model has been adopted in almost all studies, making this the state-of-the-art modelling approach.

3.1.2 Calibration of Mooney-Rivlin Material Model (Quasi-Static Loading)

Also in this study, the hyperelastic Mooney-Rivlin material model was used in Abaqus/Explicit. The strain energy potential U of this model consists of a deviatoric component and a volumetric component, which is given as follows:

$$U = C_{10}(\overline{I}_1 - 3) + C_{01}(\overline{I}_2 - 3) + \frac{1}{D_1}(J_{el} - 1)^2 \tag{3}$$

with temperature-dependent material parameters C_{10}, C_{01} and D_1 that are the input values in Abaqus/Explicit, $\overline{I}_1$ and $\overline{I}_2$ as the first and second deviatoric strain invariants and J_{el} as the elastic volume ratio. With the selection of $D_1=0$ Abaqus uses a default value for the material parameter to achieve maximum incompressibility. The two parameters C_{10} and C_{01} of the deviatoric part were calibrated using the static compression test data of the rubber impactor developed in Section 2.3. For the SHA-40 rubber the parameter C_{10} was set to 0.35 MPa, for the SHA-60 rubber to 0.90 MPa and for the SHA-80 rubber to 2.00 MPa. The parameter C_{01} is set to 0 in all cases, which results in the simplified Neo-Hookean formulation of the hyperelastic material model. Based only on compression test data, this parameter setup is suitable for compression-dominated load cases only, it might not be appropriate for more complex load cases involving tensile or combined loads.

Consequently, the first step of the rubber impactor model validation was the simulation of the quasi-static rubber impactor compression tests with a comparison to experimental data. The model was based on C3D8R solid elements with reduced integration and default hourglass control. A mesh size of 3 mm was selected as the result of a mesh convergence

study with mesh sizes from 1 to 10 mm. The rigid plate for the compression test was modelled with S4R shell elements. A surface-to-surface contact with a friction coefficient between rubber and the metallic surface of 0.78 was defined, which was experimentally determined in friction tests of aircraft tire rubber on aluminium plates in [6].

The correlation of the numerical and experimental curves for the quasi-static compression tests is in general very good. Figure 13a shows the example of the Ø40 mm SHA-60 impactor. This fact proves that the simple Mooney-Rivlin material model is very useful for this specific load case, where the level of compression strains is moderate. However, Helnwein et al. [21] as well as Karagiozova and Mines [7] remind that this simple model is only valid up to compressive strains of 50%–70%.

3.1.3 Strain Rate Effects (Dynamic Loading)

It is well-known that rubber materials exhibit a strain rate effect, i.e. the stress-strain curves are influenced by the loading rate of the material. Several experimental studies in the literature show this effect [25, 26]. Mines, McKnown and Birch [6] performed dynamic tests of aircraft tire rubber specimens in tension and compression at strain rates of 4 s^{-1}, 350 s^{-1} and 2,500 s^{-1}, showing a strong influence of the loading rate on the force levels. Hoo-Fatt and Ouyang [27] tested styrene butadiene rubber in dynamic tensile tests in the strain rate domain of 76 s^{-1} to 450 s^{-1} and found significant strain rate effects, which were covered in their Abaqus/Explicit model by viscoelastic terms. Silicone rubber with identical Shore hardness values as in the current study (SHA-40, SHA-60 and SHA-80) was tested by Shim et al. [28] in dynamic tensile and compression tests at strain rates from 10^{-2} s^{-1} to 3,300 s^{-1} on a Split-Hopkinson bar with significantly increased forces for higher loading rates. Again, the strain rate effect was covered in their numerical model by viscoelastic terms. Also the dynamic experiments with the SBS rubber impactors in the present study document this strain rate effect.

While the quasi-static material behaviour is treated by the hyperelastic law as discussed before, the rate dependency is typically included by additional viscoelasticity, making the stress state dependent on strain history or strain rate history. In Abaqus/Explicit viscoelasticity is defined by a Prony series expansion of the dimensionless relaxation modulus. The viscoelastic deviatoric and volumetric behaviour are treated independently.
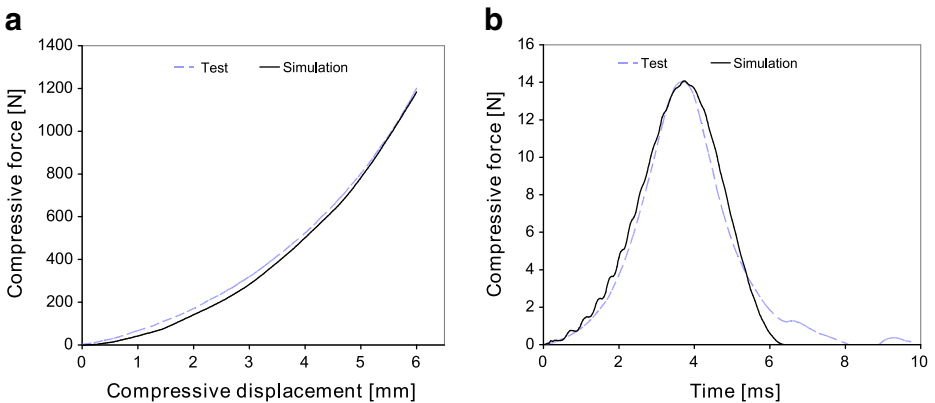

Fig. 13 Comparison of simulation and experiment (Ø40 mm, SHA-60): **a** force-displacement curves of quasi-static compression test, **b** force-time curves of low velocity impact on aluminium plate with 50 J

The parameters can either be entered directly or can be calculated from experimental test data. In the latter case, the experimental data are the input and Abaqus/Explicit automatically calculates the Prony series parameters with a least squares fit method.

The effect of the inclusion of viscoelasticity was investigated in low velocity impact simulations on the 5 mm aluminium plate described in Section 2.4. The 2024-T3 aluminium plate used in the impact tests was modelled with S4R shell elements and a mesh size of 2 mm. An elastic-plastic material model with isotropic hardening based on the tabular input of the yielding curve was used for the aluminium. Although the quasi-static model without viscoelasticity already provided results that are close to the experimental curves, the model with viscoelasticity led to shorter contact times and therefore a slightly better correlation (Fig. 13b). The high degree of compression corresponds very well to the high speed images of the test, both for the energies 50 J and 100 J. A similar correlation can also be found for the quantitative comparison of force-time and carriage displacement-time curves. As an example, the force-time curves for the Ø40 mm SHA-60 impactor for the energy of 50 J are shown in Fig. 13b. All in all, the rubber impactor model could successfully be validated for the low velocity impact simulations in this study. Generally speaking, it is recommended not to neglect strain rate effects in the rubber impactor model, especially for high velocity impact simulations.

3.2 Composite Material Modelling

Numerical analyses of 3D textile-reinforced composites on different modelling scales have been the focus of several previous studies, including detailed meso-models and homogenised macro-models [29–35]. Also in this study, two different modelling approaches for the 3D textile composite were applied: the meso- and macro-modelling approach.

3.2.1 Meso-Model of Composite Material

A detailed meso-model of the 3D textile-reinforced composite containing individual yarns and polymeric resin is useful for a general understanding of the textile architecture and stress distributions under load and can be used to obtain mechanical properties of the textile composite based on virtual tests performed on unit cell level [36–38]. In the present study, a geometrical meso-model of the 3X 55% material was generated and translated into an FE model. First approaches using general purpose software like WiseTex or TexGen were not successful, as they do not support such complex 3D textile weaves with an alternating number of weft yarns and lateral ondulations.

Therefore, an alternative, more innovative approach was applied here to generate a realistic geometrical model based on three-dimensional micro-CT scans of the textile composite as illustrated in Fig. 2. Using these data, a very accurate measurement of each yarn cross-section height, width and position is possible [39]. In order to ease the process of extracting the geometrical information from the micro-CT data and translating it to an FE model, a software tool called μCT2FEM was developed. Within this tool 2D grey-scale images are extracted from the raw micro-CT data by cutting the 3D data by planes parallel to the principal planes. Each yarn in these cross-sectional images is identified and idealised by an elliptical shape (Fig. 14). Two associated ellipses from two parallel cross-sections are then connected into a volume, a so-called yarn section, which on its turn is meshed with the FE pre-processor. In this manner, the μCT2FEM tool was used to obtain an FE model of the representative volume element (RVE) of the 3X 55% material, which is shown in
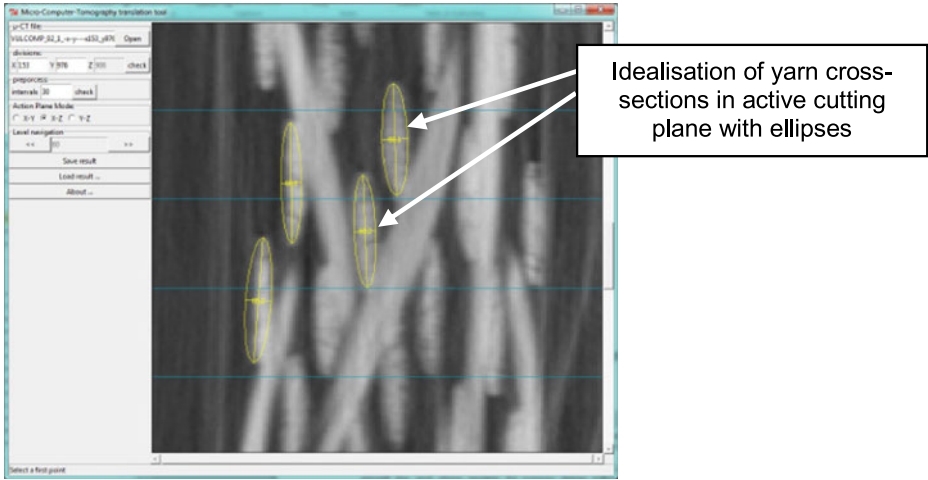
Idealisation of yarn cross-sections in active cutting plane with ellipses
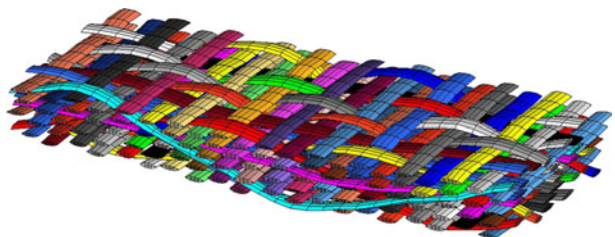
Fig. 14 User interface of µCT2FEM software tool

Fig. 15. It has to be highlighted that one single RVE of this complex textile weave has dimensions of nearly 45 mm×15 mm.

A big advantage of this method is the possibility to visualise individual yarns by blanking out others. In Fig. 16 only the 3D warp yarns are illustrated and the significant lateral ondulations are visible. Exactly this phenomenon was not possible to capture with commercial software tools. Therefore, a strong benefit is seen in the method applied here, which represents the textile structure in a much more realistic way, covering such imperfections that significantly affect the mechanical properties and damage mechanisms.

Final steps in the model generation are the definition of material properties of the yarn sections and the surrounding resin. While the resin is treated as an isotropic material with known properties of RTM6, the physical properties inside the yarns are dependent on the local fibre volume fraction and must therefore be calculated separately for each yarn section. For the elastic properties of the yarns the Chamis mixing formulae [40] were used and the linear coefficients of thermal expansion and density were taken from Schürmann [41]. The local fibre volume fraction V_f inside a yarn section is calculated based on its surrounding elliptical cross-section using:

$$V_f = \frac{N_f d_f^2}{d_1 d_2} \tag{4}$$

Fig. 15 FE mesh of dry 3X 55% textile weave RVE
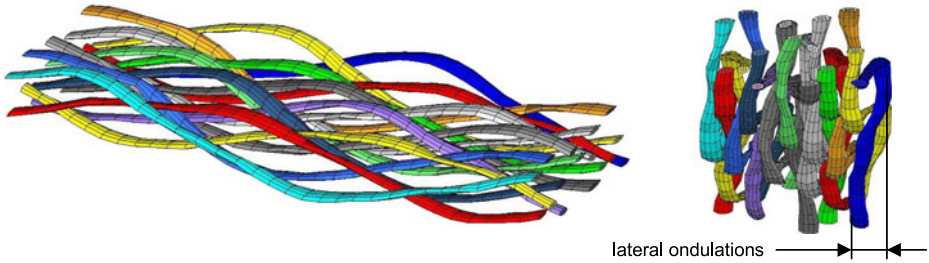
lateral ondulations →   ←

Fig. 16 Illustration of the 3D warp yarns and the significant lateral ondulations

where N_f is the number of filaments in a roving (12,000 in a roving used in the 3X 55% weave), d_f the diameter of a single filament (7 µm is assumed) and d_1 and d_2 the average size of the major and minor axis of the two surrounding elliptical yarn cross-sections.

The meso-model of the 3X 55% material in this study was primarily built to gain information on the distribution of the yarns in this complex 3D textile weave and to identify imperfections and their influence on the mechanical properties. Without question, it would numerically be too expensive to be used for impact simulations on current computer systems, although a very detailed analysis of stress distributions and failure mechanisms could be possible. Therefore, the development of a homogenised macro-model of the textile composite was necessary in order to perform efficient impact simulations.

3.2.2 Macro-Model of Composite Material

The purpose of the macro-model is to represent the homogenised global behaviour of the 3D textile-reinforced material correctly, both in terms of elastic and damage properties, using either shell or solid elements for the homogenised material. In the present study, the decision fell on S4R shell elements. On the one hand, this is a strong simplification, neglecting any stresses in z-direction especially under impact loads, but on the other hand it reflects the typical modelling approach of thin-walled composite structures. In aircraft engineering, there is a strong demand of efficient numerical methods, allowing for reduced development times. Using 3D elements, which would be the more accurate method, would virtually eliminate the model for a utilisation in large-scale aeronautic structures due to the high computational cost. Efficient multiscale modelling methods, which combine detailed models in the local impact zone with coarse global models of the large-scale structure, are under development but not mature yet. Therefore, the aim here was to investigate, if this simplified modelling approach is able to represent the impact performance of the 3D textile composite in an acceptable manner with a potential of utilisation in large-scale structures.

Of key importance in this modelling approach is the constitutive law used for the homogenised elements. Both the elastic behaviour and the damage progression have to be covered by the model. In the present study, a continuum damage mechanics model was adopted, which is based on the Ladeveze model for unidirectional plies [42–45] and extended for textile fabrics by Johnson and Simon [46], implemented as a VUMAT user subroutine in Abaqus/Explicit. The constitutive stress-strain relations are formulated in a local Cartesian coordinate system with base vectors aligned with the warp and weft directions. The textile-reinforced ply is modelled as a homogeneous orthotropic elastic

material with the potential to sustain progressive stiffness degradation due to fibre/matrix cracking and plastic deformation under shear loading. Based on the local coordinate system with the fibre directions in 1- and 2-direction, the elastic relation is defined as:

$$
\begin{pmatrix} \varepsilon_{11} \\ \varepsilon_{22} \\ \varepsilon_{12}^{el} \end{pmatrix} = \begin{pmatrix} \dfrac{1}{(1-d_1)E_1} & \dfrac{-v_{12}}{E_1} & 0 \\ \dfrac{-v_{21}}{E_2} & \dfrac{1}{(1-d_2)E_2} & 0 \\ 0 & 0 & \dfrac{1}{(1-d_{12})2G_{12}} \end{pmatrix} \begin{pmatrix} \sigma_{11} \\ \sigma_{22} \\ \sigma_{12} \end{pmatrix} \tag{5}
$$

The damage variables d_1 and d_2 are introduced, which are associated to fibre fracture in 1- and 2-directions, respectively, with a differentiation between tensile and compressive fibre failure modes. These fibre damage variables depend only on the corresponding thermodynamic force. Failure in fibre directions is controlled by tensile or compressive strength values. The post-damage behaviour is a function of the damage thresholds and fracture energies per unit area under uniaxial tensile or compressive loading. The shear response of the textile composite is mainly dominated by the nonlinear behaviour of the matrix material, which includes both plasticity and stiffness degradation due to matrix micro-cracking expressed by damage variable d_{12}. Further details of the model and mechanical formulae can be found in [46].

The calibration of the parameters of the material model was based on the experimental test results of the coupon tests of the 3D textile composite as described before. Almost all of these parameters could directly be taken from the test data. Most effort had to be put into the calibration of the shear response with plasticity and damage progression using the cyclic 45° tensile test data. The increasing level of damage could be measured from the ratio of the unloading stiffness to the initial undamaged elastic stiffness. The calibration of the parameters of the hardening curve was based on the evaluation of the increasing values of residual deformation in the unloaded state for each unloading curve.

In order to validate the final composite macro-model, the coupon tests were simulated with Abaqus/Explicit. The correlation of the experimental and numerical curves is shown in Fig. 17. The correlation for low and medium strain values until about 0.6% is very satisfying. Beyond that, certain characteristics of the experimental curves like nonlinearities or plateau stresses in warp and weft direction cannot be covered by the model, which
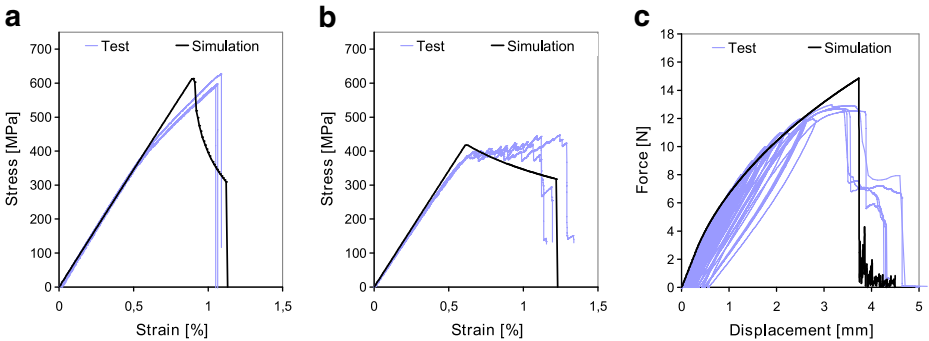

Fig. 17 Comparison of simulation and experiment: **a** tensile tests in warp direction, **b** tensile test in weft direction, **c** 45° tensile test

appears to overestimate the stiffness. But it can be stated that the correlation of test and simulation model is acceptable so that this model was used for the impact simulations on composite plates.

3.3 Impact Simulations

The impact simulations were performed with the 3X 55% textile-reinforced composite material and the Ø40 mm SHA-60 rubber impactor. Both the rubber impactor model and composite material model that were validated individually were adopted without changing any parameters. The 100 mm×100 mm×2.7 mm composite plate was meshed with 2 mm S4R shell elements with enhanced hourglass control. At the border of the Ø70 mm window all nodes were fixed in z-translation and the clamped outer surface was completely fixed in x-, y- and z-translation, representing the experimental clamping device. Gravity was included and an initial velocity correlating to the impact energy was ascribed to the impactor. All five impact energies 50 J, 63 J, 75 J, 88 J and 100 J representing the drop heights from 1 m to 2 m were simulated. A total simulation time of 10 ms was chosen, leading to approx. 30 min CPU time per simulation.

Figure 18 shows an image sequence of the impact simulation with the highest impact energy of 100 J. The plate deflects for several millimetres but does not fail globally. Some plastic deformation remains after spring-back of the rubber impactor. Only 10% of the initial kinetic energy are absorbed by the composite plate, 90% are stored in the elastic deformation and transformed into residual spring-back velocity. For 50 J even 97% of the initial energy remain as residual kinetic energy. This is a major difference of rubber impacts compared to hard body impact loads with rigid impactors, where the impactor itself typically does not store any elastic energy.

The displacement-time curves in the simulation and experiment for 50 J and 100 J match relatively well, see Fig. 19b. A tendency can be seen that the simulation curves are in general slightly lower. The correlation of the force-time curves in Fig. 19a is worse. The numerically predicted force values are significantly higher, although the overall contact time is similar. Higher contact forces are typically caused by higher stiffness values of the target. Therefore, one explanation might be the higher numerical stiffness of the composite plate for strains higher than 0.6%, see Fig. 17a. This theory is supported by the fact that the force and displacement curves in Fig. 19 match well in the beginning and the difference only appears for higher deformations. This would make a different constitutive modelling of the composite plate necessary. It can also be possible that the two-dimensional modelling is insufficient because of the neglect of through-thickness damage mechanisms such as yarn decohesions seen in Fig. 12, which may reduce the contact bending stiffness. Another explanation might be the high compressive strains of the rubber. The impactor model was only validated for moderate compressive strains, but here the compression is much higher.
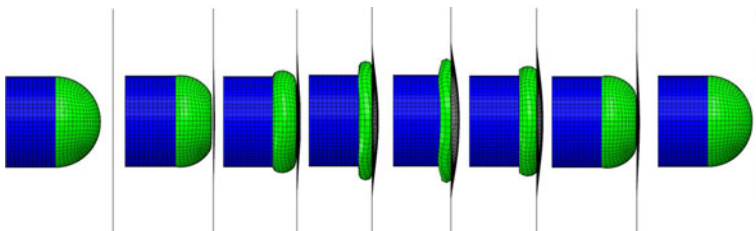

Fig. 18 Image sequence of rubber impact simulation on composite plate with impact energy of 100 J
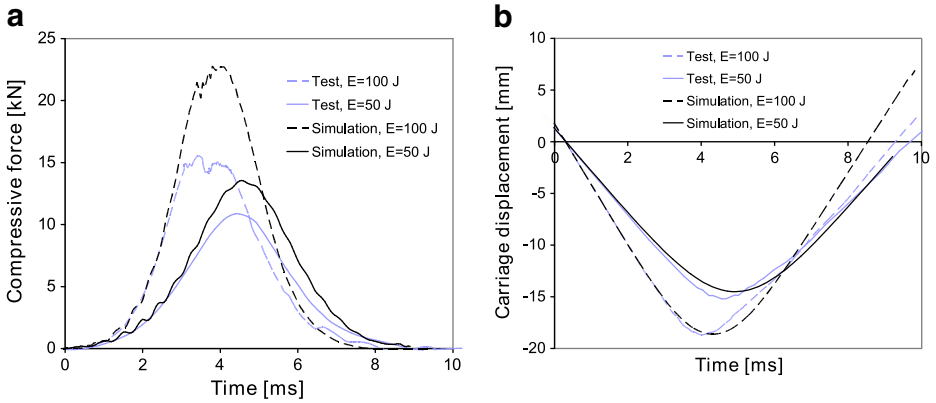
Fig. 19 Comparison of simulation and experiment: **a** force-time curves and **b** carriage displacement-time curves for SHA-60 rubber impact on 3X 55% composite plates

Also the boundary conditions in the simulation might be a cause for inaccuracies. The outer edges of the plate model are completely fixed resulting in a rigid support. In the test there might be some minimal slippage or elasticity, leading to these differences.

The assessment of the damage in the composite plate is shown in Fig. 20. The five damage parameters of the composite material model for tensile and compressive damage in warp and weft direction plus shear damage have been plotted at the simulation state of 10 ms. All images have the same legend with values ranging from 0 to 1. For

Fig. 20 Comparison of simulation and experiment: damage in 3X 55% composite plate

comparison reasons, the experimental thermography images of the 3X 55% material are also shown. However, a comparison is relatively difficult, because first of all it is not clear what exact kind of damage can be seen in these thermographic images and secondly the simulation result images strongly depend on the legend chosen. Therefore, only the general findings are compared. It can be seen that two independent areas of damage exist: the damage directly at the point of impact in the plate middle and the circular damage at the boundary of the clamping window. These damages are visible both in simulation and experiment. It can also be seen that the damage increases with increasing impact velocity. For the lowest velocities, no damage in the strong direction 1 occurs, only in the weaker direction 2. Some shear damage is visible even for the lowest velocities.

All in all, the general correlation between test and simulation appears to be promising, although some differences especially in the force curves are visible.

4 Conclusions

A low velocity impact study of aircraft tire rubber on 3D textile-reinforced composite plates was performed experimentally and numerically. In contrast to regular unidirectional composite laminates, no delaminations occur in such a 3D textile composite because the plate consists of only one ply of the textile weave. Yarn decohesions, matrix cracks and few yarn ruptures, typically located at the back side of the 2.7 mm thin plates, have been identified as the major damage mechanisms under the normal impact load. The higher the ratio of 3D warp yarns to straight warps is selected, the lower the impact damage is. The composite plates with 100% 3D warp yarns in this study showed the smallest extent of damage. However, such a textile with this high amount of ondulated yarns has reduced inplane stiffness properties compared to a weave with more straight warp yarns. Therefore, good impact damage tolerance and good stiffness properties appear to be oppositional in this 3D textile composite material.

Numerical simulation models of the textile weave have been developed on the meso- and macro-scale. The rubber impactor was modelled with the hyperelastic Mooney-Rivlin constitutive law. A step-by-step validation with static rubber compression tests and low velocity impact tests on aluminium plates led to a reliable impactor model. It was learned that the relatively simple Mooney-Rivlin model is appropriate for such low velocity impact loads with moderate compression states. Viscoelastic terms should be added in order to cover strain rate effects at higher loading rates. The correlation between impact simulation results and test data was in general promising with some differences in the force curves. This was attributed to the limitations and simplifications of the shell model and boundary conditions.

The characteristic of a rubber impact compared to a hard body impact at low velocity is the high amount of elastic energy stored in the impactor during impact. More than 90% of the initial kinetic energy were returned as residual kinetic energy of the rubber impactor after spring-back. Consequently, the geometrical deformation of the rubber during impact is also significant, making the impact load less localised than in a hard body impact load case. The next step will be the extension of this study for high velocity impact loads.

References

1. Mouritz, A.P., Bannister, M.K., Falzon, P.J., Leong, K.H.: Review of applications for advanced three-dimensional fibre textile composites. Compos. A **30**(12), 1445–1461 (1999)
2. Byun, J.H., Um, M.K., Hwang, B.S., Song, S.W.: Impact performance of 3D interlock textile composites. In: Composites Technologies for 2020, Ye, L., Mai, Y.W., Su, Z. (eds.) Proceedings of 4th Asian-Australasian Conference on Composite Materials (ACCM-4), Sydney, Australia, July 6–7, 2004
3. Lv, L., Sun, B., Qiu, Y., Gu, B., Gu, B.: Energy absorptions and failure modes of 3D orthogonal hybrid woven composite struck by flat-ended rod. Polymer. Compos. **27**(4), 410–416 (2006)
4. Hu, H., Sun, B., Sun, H., Gu, B.: A comparative study of the impact response of 3D textile composites and aluminium plates. J. Compos. Mater. **44**(5), 593–619 (2010)
5. Byers, A.: The Crash of the Concorde. The Rosen Publishing Group, Inc., New York (2003)
6. Mines, R.A.W., McKnown, S., Birch, R.S.: Impact of aircraft rubber tyre fragments on aluminium alloy plates: I—Experimental. Int. J. Impact Eng. **34**(4), 627–646 (2007)
7. Karagiozova, D., Mines, R.A.W.: Impact of aircraft rubber tyre fragments on aluminium alloy plates: II—Numerical simulation using LS-DYNA. Int. J. Impact Eng. **34**(4), 647–667 (2007)
8. Birch, R.S., Bergler, C., Kracht, M., Karagozova, D., Mines, R.A.W.: Post-test simulation of airliner wing access panel subject to tyre debris impact. 5th European LS-DYNA Users Conference, Birmingham, UK, May 25–26, 2005
9. Hörmann, M.: FE-application in aircraft structure analysis. 10th International LS-DYNA Users Conference, Dearborn, MI, June 8–10, 2008
10. Toso-Pentecote, N., Johnson, A.F., Chabrier, G.: Modelling and simulation of tyre impacts on stiffened composite panels. Composites 2009, 2nd ECCOMAS Thematic Conference on the Mechanical Response of Composites, London, April 1–3, 2009
11. Toso-Pentecote, N., Schwinn, D., Johnson, A.F.: Modelling and simulation of tyre impacts on stiffened composite panels. SAMPE Europe International Conference, Paris, April 12–14, 2010
12. Dau, F., Duplessis Kergomard, Y.: Study on interlock 3X damage mechanisms under impact loading using a deformable impactor. 14th International Conference on Experimental Mechanics (ICEM 14), Poitiers, France, July 4–9, 2010
13. Duplessis Kergomard, Y., Dau, F., Heimbs, S., Besnard, G., Hild, F.: Study on interlock 3X damage mechanisms under impact loading using a deformable impactor. 17èmes Journées Nationales sur les Composites (JNC 17), Poitiers, France, June 15–17, 2011
14. Mooney, M.: A theory of large elastic deformation. J. Appl. Phys. **11**(9), 582–592 (1940)
15. Rivlin, R.S.: Large elastic deformations of isotropic materials. I. Fundamental concepts. Phil. Trans. Roy. Soc. Lond. **A240**, 459–490 (1948)
16. Johnson, A.F., Kempe, G., Simon, J.: Design of composite wing access cover under impact loads. Appl. Compos. Mater. **7**(4), 219–229 (2000)
17. Neves, R.R.V., Micheli, G.B., Alves, M.: An experimental and numerical investigation on tyre impact. Int. J. Impact Eng. **37**(6), 685–693 (2010)
18. Bolarinwa, E.O., Olatunbosun, O.A.: On rubber material properties for FE tyre model. Proceedings of the Ninth Annual Postgraduate Research Symposium, pp. 21–25. University of Birmingham, UK (2003)
19. Bolarinwa, E.O., Olatunbosun, O.A.: Finite element simulation of the tyre burst test. Proc. Inst. Mech. Eng. **218, Part D**, 1251–1258 (2004)
20. Reid, J.D., Boesch, D.A., Bielenberg, R.W.: Detailed tire modeling for crash applications. Int. J. Crashworthiness **12**(5), 521–529 (2007)
21. Helnwein, P., Liu, C.H., Meschkie, G., Mang, H.A.: A new 3-D finite element model for cord-reinforced rubber composites—application to analysis of automobile tires. Finite Elem. Anal. Des. **14**(1), 1–16 (1993)
22. Nguyen, S.N., Greenhalgh, E.S., Olsson, R., Iannucci, L., Curtis, P.T.: Modeling the lofting of runway debris by aircraft tires. J. Aircraft **45**(5), 1701–1714 (2008)
23. Nguyen, S.N., Greenhalgh, E.S., Iannucci, L., Olsson, R., Curtis, P.T.: Improved models for runway debris lofting simulations. Aeronaut. J. **113**(1148), 669–681 (2009)
24. Nguyen, S.N., Greenhalgh, E.S., Olsson, R., Iannucci, L., Curtis, P.T.: Parametric analysis of runway stone lofting mechanisms. Int. J. Impact Eng. **37**(5), 502–514 (2010)
25. Song, B., Chen, W.: One-dimensional dynamic compressive behaviour of EPDM rubber. J. Eng. Mater. Tech. **125**(3), 294–301 (2003)
26. Yang, L.M., Shim, V.P.W., Lim, C.T.: A visco-hyperelastic approach to modeling the constitutive behaviour of rubber. Int. J. Impact Eng. **24**(6–7), 545–560 (2000)
27. Hoo Fatt, M.S., Ouyang, X.: Three-dimensional constitutive equations for styrene butadiene rubber at high strain rates. Mech. Mater. **40**(1–2), 1–16 (2008)

28. Shim, V.P.W., Yang, L.M., Lim, C.T., Law, P.M.: A visco-hyperelastic constitutive model to characterize both tensile and compressive behaviour of rubber. J. Appl. Polymer Sci. **92**(1), 523–531 (2004)
29. Li, Z., Sun, B., Gu, B.: FEM simulation of 3D angle-interlock woven composite under ballistic impact from unit cell approach. Comput. Mater. Sci. **49**(1), 171–183 (2010)
30. Naik, N.K., Azad, S.N.M., Durga Prasad, P., Thuruthimattam, B.J.: Stress and failure analysis of 3D orthogonal interlock woven composites. J. Reinforc. Plast. Compos. **20**(17), 1485–1523 (2001)
31. Nauman, S., Boussu, F., Legrand, X., Koncar, V.: Geometrical modelling of 3D interlock fabric. 13th European Conference on Composite Materials (ECCM-13), Stockholm, Sweden, June 2–5, 2008
32. Schneider, J., Marcin, L., Aboura, Z., Marshal, D.: Experimental investigation and behaviour modeling of a 3D interlock woven fabric composite: part 1. In: Recent Advances in Textile Composites, Advani, S. G. (ed.) Proc. 9th International Conference on Textile Composites, Newark, DE, Oct. 13–15, 2008
33. Marcin, L., Schneider, J., Kaminski, M., Maire, J.F., Marsal, D.: Experimental investigation and behaviour modeling of a 3D interlock woven fabric composite: part 2. In: Recent Advances in Textile Composites, Advani, S.G. (ed.) Proc. 9th International Conference on Textile Composites, Newark, DE, Oct. 13–15, 2008
34. DeLuycker, E., Morestin, F., Boisse, P., Marsal, D.: Simulation of 3D interlock composite preforming. Compos. Struct. **88**(4), 615–623 (2009)
35. Bogdanovich, A.E.: Progressive failure modeling and strength predictions of 3-D woven composites. In: Recent Advances in Textile Composites, Advani, S.G. (ed.) Proc. 9th International Conference on Textile Composites, Newark, DE, Oct. 13–15, 2008
36. Van Den Broucke, B., Colin de Verdiere, M., Hartung, D., Middendorf, P., Pickett, A., Ranz Angulo, D., Schouten, M., Tessmer, J.: Failure and impact modelling of textile composites: ITOOL project. SAMPE Europe 28th International Conference, Paris, April 2–4, 2007
37. Van Den Broucke, B., Middendorf, P., Lomov, S.V., Verpoest, I.: Modelling of damage in textile reinforced composites: micro-meso approach. Proceedings of Symposium on Finite Element Modeling of Textiles and Textile Composites, St. Petersburg, Russia, September 26–28, 2007
38. Van Den Broucke, B., Hamila, N., Middendorf, P., Lomov, S.V., Boisse, P., Verpoest, I.: Determination of the mechanical properties of textile-reinforced composites taking into account textile forming parameters. Int. J. Mater. Form. **3**(2), 1351–1361 (2010)
39. Linde, P., Middendorf, P., Van Den Broucke, B., De Boer, H.: Numerical simulation of damage behaviour of textile reinforced composites in aircraft structures. 27th Congress of the International Council of the Aeronautical Sciences (ICAS 2010), Nice, France, September 19–24, 2010
40. Chamis, C.: Mechanics of composite materials: past, present and future. J. Compos. Tech. Res. **11**(1), 3–14 (1989)
41. Schürmann, H.: Konstruieren mit Faser-Kunststoff-Verbunden. Springer, Berlin (2007)
42. Dumont, J.P., Ladeveze, P., Poss, M., Remond, Y.: Damage mechanics for 3-D composites. Compos. Struct. **8**(2), 119–141 (1987)
43. Ladeveze, P., Le Dantec, E.: Damage modelling of the elementary ply for laminated composites. Compos. Sci. Tech. **43**(3), 257–267 (1992)
44. Ladeveze, P.: A damage mesomodel of laminate composites. In: Lemaitre, J. (ed.) Handbook of Materials Behaviour Models, Section 10.6, vol. 3, pp. 1004–1014. Publisher Academic Press (2001)
45. Lubineau, G., Ladeveze, P.: Construction of a micromechanics-based intralaminar mesomodel, and illustrations in ABAQUS/Standard. Comput. Mater. Sci. **43**(1), 137–145 (2008)
46. Johnson, A.F., Simon, J.: Modelling fabric reinforced composites under impact loads. In: Euromech 400: Impact and Damage Tolerance of Composite Materials and Structures. London, September 27–29, 1999